International Journal of Biological Macromolecules 375 (2026) 153416

Contents lists available at ScienceDirect

International Journal of Biological Macromolecules

journal homepage: www.elsevier.com/locate/ijbiomac

CTAB-modified chitosan nanocoatings: Increasing the cationic surface character by self-assembly

Péter Márton [a,b,*], Petra Demény [a], Adél Rácz [b], Tamás Szabó [c], Zsófia Keresztes [c], Bence Balterer [d], János Madarász [e], Norbert Nagy [b], Rita Márton [f], Mónika Molnár [f], Zoltán Hórvölgyi [a,**]

[a] Department of Physical Chemistry and Materials Science, Faculty of Chemical Technology and Biotechnology, Budapest University of Technology and Economics, Műegyetem rkp. 3., H-1111, Budapest, Hungary
[b] Institute of Technical Physics and Materials Science, HUN-REN Centre for Energy Research, Konkoly-Thege Miklós út 29-33, H-1121, Budapest, Hungary
[c] Functional Interfaces Research Group, Institute of Materials and Environmental Chemistry, HUN-REN Research Centre for Natural Sciences, Magyar tudósok körútja 2, Budapest, 1117, Hungary
[d] NMR Research Laboratory, Centre for Structural Science, HUN-REN Research Centre for Natural Sciences, Magyar Tudósok krt. 2, H-1117, Budapest, Hungary
[e] Department of Inorganic and Analytical Chemistry, Faculty of Chemical Technology and Biotechnology, Budapest University of Technology and Economics, Műegyetem rkp. 3, H-1111, Budapest, Hungary
[f] Department of Applied Biotechnology and Food Science, Faculty of Chemical Technology and Biotechnology, Budapest University of Technology and Economics, Műegyetem rkp. 3, H-1111, Budapest, Hungary

ARTICLE INFO

Keywords:
Chitosan
Nanocoating
Cetyltrimethylammonium bromide
Polymer-surfactant interactions
Cationic surface character

ABSTRACT

Cetyltrimethylammonium bromide (CTAB)-containing chitosan nanolayers were deposited onto glass substrates via dip-coating from aqueous precursor solutions with 1% chitosan and 0–3.0 mM CTAB content. The thickness of the coatings was ca. 200–300 nm, according to UV–visible spectroscopy. While lower surfactant concentrations (0.25–1.0 mM) resulted in homogeneous, semicrystalline coatings, AFM, X-ray diffraction and solid-state NMR evidenced phase separation and the formation of CTAB crystallites in the case of the samples made from precursor solutions with over 1.0 mM CTAB concentration. X-ray photoelectron spectroscopy confirmed a significant interfacial accumulation of CTAB on the coating-air interface (up to eightfold increase in quaternary N), while contact angle measurements indicated an increase in hydrophilicity, with advancing water contact angles decreasing from 70° to ca. 30°, with increasing Lewis-basic surface free energy component. Crucially, surface zeta potential measurements demonstrated an increase in positive surface charge from +22 mV to over +30 mV, and turbidimetric and colorimetric assays confirmed the antibacterial effect (over 80% inhibition) of the coatings against *B. subtilis*. These findings suggest the formation of a unique molecular structure, where the CTAB was accumulated on the surface of the nanolayer with outward-oriented cationic head groups, providing a robust strategy for developing enhanced antimicrobial coatings.

1. Introduction

Chitosan (CS), a versatile biopolymer derived from the partial alkaline deacetylation of chitin [1], has garnered significant attention in fields ranging from the food industry to biomedicine due to its biocompatibility, biodegradability and pH-responsive nature [2–5]. Its hydroxyl and amino groups make it a good complexing agent, so it is often used to bind metal ions (e.g. harmful heavy metals [6]) or as a capping agent in the production of nanoparticles [7–9]. In medical applications (e.g. wound healing), the antibacterial effect of CS is a critical factor, which is primarily due to its cationic nature originating from the protonation of free amino groups along the polymer backbone [10]. This property facilitates the adsorption of the polymer onto the bacterial cell walls – which contain mainly anionic or electron donating moieties – leading to membrane disruption and cell death [11]. Similarly, cetyltrimethylammonium bromide (CTAB), a well-known cationic surfactant

* Correspondence to: P. Márton, Department of Physical Chemistry and Materials Science, Faculty of Chemical Technology and Biotechnology, Budapest University of Technology and Economics, Műegyetem rkp. 3., H-1111, Budapest, Hungary.
** Corresponding author.
E-mail addresses: marton.peter@vbk.bme.hu (P. Márton), horvolgyi.zoltan@vbk.bme.hu (Z. Hórvölgyi).

https://doi.org/10.1016/j.ijbiomac.2026.153416
Received 24 February 2026; Received in revised form 1 July 2026; Accepted 7 July 2026
Available online 9 July 2026
0141-8130/© 2026 The Authors. Published by Elsevier B.V. This is an open access article under the CC BY-NC-ND license (http://creativecommons.org/licenses/by-nc-nd/4.0/).

and antiseptic [12], exhibits a comparable antibacterial mechanism by interacting with membrane proteins via its quaternary ammonium head group, inactivating them [13,14]. Due to its high efficiency, it can also be used as an active component of antibacterial coatings or surfaces [15].

In aqueous systems containing polyelectrolytes and surfactants, the structural organization is governed by the delicate balance between electrostatic repulsion and hydrophobic attraction [16]. CTAB can interact with polar neutral or anionic polymers and bind them in the outer (Stern) layer of micelles, which can be exploited in many industrial applications [17]. However, in the case of CS, since the polymer and the surfactant have the same charge electrostatic repulsion occurs, so only hydrophobic interactions between the non-polar segments of chitosan and the carbon chains of the surfactant can facilitate the association, which has been demonstrated by several researchers [18,19]. Instead of classical solubilization, this results in the formation of associates in an aqueous medium where the hydrophobic tail interacts with the nonpolar parts of the polymer molecule and the polar head group faces outward (bottle-brush structure or worm-like micelles) [16,20]. We hypothesize that preserving this specific supramolecular arrangement during the solvent evaporation process allows the fabrication of polymer films with distinct surface properties. Specifically, the outward-facing CTAB head groups could significantly amplify the polarity and cationic charge of the surface. To the best of our knowledge, the study of the bulk and surface structures of nanocoatings prepared from CS-CTAB solutions, as well as systematic surface studies (including surface free energy, zeta potential and morphology measurements), has not been performed previously. Furthermore, no data is currently available regarding the antibacterial properties of combined CS-CTAB coatings.

In this study, nanocoatings were prepared from CS solutions containing different amounts of CTAB onto glass substrates via dip-coating technique. The optical properties and composition of the coatings were studied by X-ray diffraction, UV–Visible-, NMR- and X-ray photoelectron spectroscopy. The surface properties (e.g. polarity or charge) resulting from the structure of the aforementioned polymer-surfactant associates were studied by wettability tests (surface energy assessment), AFM and surface zeta potential measurements to determine the quality and quantity of functional groups on the surface. Based on the known antimicrobial characteristics of both components, the antibacterial effect of the coatings was systematically evaluated against the Gram-positive bacterium *Bacillus subtilis* using turbidimetric and colorimetric assays. The demonstrated tunability of surface charge based on the synergistic effect of CS and CTAB offers a promising avenue for developing next-generation green antimicrobial coatings.

2. Methods

2.1. Reagents

Chitosan powder (CS, viscosity-average molecular weight: 388 kDa, 83% degree of deacylation, for the measurement of these data see section S1 in Appendix), sodium acetate (NaAc, 99.0% f.a.), diiodomethane (ReagentPlus®, 99%, contains copper as stabilizer) and formamide (ReagentPlus®, 99.0%) were purchased from Merck (Germany). Isopropyl alcohol (iPrOH, 99.7%, f.a.) cetyltrimethylammonium bromide (CTAB, 99%, f.a.) and sodium chloride (NaCl, 99.5%, f.a.) were provided by Reanal (Hungary), acetic acid (AcOH, 99.8%, f.a.) by Lachner (Czech Republic), sulfuric acid (H_2SO_4, 96%, f.a.) by Carlo Erba (Italy) and 3-(4,5-dimethylthiazol-2-yl)-2,5-diphenyl tetrazolium bromide (MTT) by Thermo Fisher Scientific Inc. (USA). All chemicals were used as received without any further purification. Aqueous solutions were made with ultrapure water (specific electrical resistance: 18.2 MΩ·cm, produced with an Adrona Integrity+ device).

2.2. Coating preparation

The glass substrates were cleaned with aqueous detergent solution, 10% H_2SO_4, iPrOH and ultrapure water before the sample preparation. The CTAB-containing CS solutions were prepared by mixing 1.5 m/m% CS solution (made by dissolving 1.5 g CS powder in 97 mL 1.5 v/v% aqueous AcOH solution then centrifuged at 4000 rpm for 30 min with a HERMLE Z36 HK device) and CTAB solutions (used in different concentrations, made by dissolving the appropriate amount of solid surfactant in ultrapure water) in 2:1 volume ratio and stirred for 1 h at room temperature. In the final precursor solutions, the CS concentration was kept at 1 m/m% in all cases, and the CTAB concentration was 0 mM, 0.25 mM, 0.5 mM, 1.0 mM, 1.5 mM or 3.0 mM. The nanocoatings were prepared on glass substrates via dip-coating with a device made by Plósz Mérnökiroda Kft. (Budapest, Hungary) at 25 °C, with a 5 cm/min withdrawal speed, and dried for 24 h at ambient conditions. Cast films were made by pouring 10 mL of the same precursor solutions into circular silicone molds and allowing them to dry at ambient conditions for a week. The cast films were chopped into approximately 1 × 2 mm pieces for XRD and NMR studies.

For coatings applied to glass substrates, the following notation is used: Gls/CS(Y mM), where "Gls" denotes the glass substrate and "Y" denotes the CTAB concentration of the precursor solution. For cast films, the notation is similar, but "Gls" is not included. For example, Gls/CS (1.0 mM) denotes a nanocoating formed on a glass substrate via dip-coating from a precursor solution containing 1 m/m% CS and 1.0 mM CTAB, while CS(1.0 mM) denotes a film cast from the same precursor solution.

2.3. Surface tension measurements

To investigate the surface properties of the precursor solutions and the possible CS-CTAB interactions, surface tension measurements were carried out with the pendant drop method using a Drop Shape Analysis System (DSA30, Krűss GmbH, Hamburg, Germany). The shape of the droplet was analysed by the software of the device (ADVANCE 1.15.0), assuming that the density of precursor solutions equals the density of ultrapure water. All surface tension value was determined from the data of at least ten droplets ($n = 10$).

2.4. UV–visible spectroscopy

To study the optical properties and determine the thickness of the nanocoatings UV–Visible spectroscopic measurements were carried out with an Analytik Jena Specord 200 UV–Vis spectrophotometer (Analytik Jena GmbH, Jena, Germany) in the 350–1050 nm wavelength range. The thickness and refractive index of the coatings was determined using a thin-layer optical model (Hild-model), a detailed description of which can be found in Ref. [21,22]. Data points were calculated from the fitted values of six replicate samples ($n = 6$).

2.5. Contact angle measurements and surface free energy calculation

To characterize the wettability and surface free energy of the surface of the coatings, contact angle measurements were carried out with ultrapure water, diiodomethane and formamide with a Drop Shape Analysis System (DSA30, Krűss GmbH, Hamburg, Germany). Contact angles were measured on the surfaces using the sessile drop method and the drop-build-up technique. A 10 uL droplet of the measuring liquid was placed to the surface at 25 °C and at least 80% relative humidity in a closed chamber, and the advancing contact angles were determined immediately with the software of the device (ADVANCE 1.15.0). At least 12 contact angle values (6 droplets, left and right angle) were measured for every coating ($n = 12$). For preliminary stability studies the coatings were soaked in ultrapure water for 10 min, dried under ambient conditions, and then the water contact angle measurements were repeated

as above.

The total surface free energy and its components were determined using the van Oss model (LW-AB approach) [23]. According to this, the surface free energy can be divided into two components: the Lifshitz–van der Waals component (γ^{LW}, describing the effect of Van der Waals interactions) and an acid–base component (γ^{AB}) describing the interactions of the electron acceptor-electron donor moieties. γ^{AB} can be expressed as the function of these electron acceptor (γ^{+}) and electron donor (γ^{-}) components (Eq. (1)).

$$\gamma^{AB} = 2\sqrt{\gamma^{+}\gamma^{-}} \tag{1}$$

The calculation of the surface free energy components of the solid surface requires contact angle measurements with three different liquids with known surface tension components. The obtained data can be substituted into the model, yielding three equations that include the above factors (Eq. (2)). The system of equations can then be solved for the surface energy components of the solid surface.

$$\gamma_{lv}(1+\cos\Theta_A) = 2\sqrt{\gamma_{sv}^{LW}\gamma_{lv}^{LW}} + 2\sqrt{\gamma_{sv}^{+}\gamma_{lv}^{-}} + 2\sqrt{\gamma_{sv}^{-}\gamma_{lv}^{+}} \tag{2}$$

where *s*, *l* and *v* subscripts denote the solid, liquid and vapor phases respectively and Θ_A is the advancing contact angle of the measuring liquid. The surface tension components of water, diiodomethane and formamide were used from Ref. [24].

2.6. AFM measurements

AFM images were recorded in tapping mode with an AIST-NT SmartSPM 1000 AFM device and NanoSensors PPP-NCHR-20 tip (nominal radius < 20 nm) to study the surface morphology of the coatings. Height and phase images were recorded in 5 × 5 and 20 × 20 μm areas. The data were evaluated with the Gwyddion 2.66 software [25].

2.7. Surface zeta potential measurements

Zeta potential (ZP) and surface zeta potential (SZP) measurements were carried out with a Malvern Zetasizer Nano ZS instrument (Malvern Instruments Ltd., Malvern, Worcestershire, UK), using a ZEN1020 type surface zeta potential measurement cell (Malvern Panalytical Ltd., Malvern, Worcestershire, UK) and disposable plastic cuvettes (DTS0012, Malvern Panalytical) with the method reported by Corbett et al. [26]. For the measurements 4×5 mm pieces were cut from the coatings on glass substrates and glued onto the PEEK (polyetheretherketone) sample holders (ZEN4060, Malvern Panalytical). The samples then were mounted on the SZP-measuring cell and submerged into the disposable plastic cuvette filled with 1.0 mL pH = 6 AcOH-NaAc buffer. The buffer was made by dissolving 0.6442 g NaAc and 15.2 μL AcOH in 100 mL ultrapure water. 10 μL suspension of aminated SiO_2 tracer particles (Size: 0.234 ± 0.01 μm; NH_2 > 30 μmol/g; 5% w/v aqueous suspension; microParticles GmbH, Berlin, Germany) were added to the buffer.

Each measurement consisted of a distance-dependent ZP measurement of the tracer particles, and a regular ZP measurement at a distance where the tracer particles are free from the electrostatic effect of the coating surface. During the distance-dependent program the ZP was measured three times at each of the 125, 250, 375 and 500 μm positions (distance from the coating surface); and at the sample-independent position (1000 μm) as well. Between every measurement a 10 s waiting period was left. One measurement consisted of 10–15 records, lasting for 5–10 s (within these ranges the execution, including the applied voltage was set to automatic). Data acquisition and processing was made via Zetasizer software (ver. 7.11). For zeta potential calculations Smoluchowski approximation was applied to Henry's equation. All measurements were carried out at 25 °C. When switching samples, the SZP measurement cell was thoroughly cleaned with ethanol and ultrapure water.

2.8. X-ray photoelectron spectroscopy

To reveal the in-depth composition of the coatings, XPS cluster depth profiling was applied in a Thermo Scientific ESCALAB Xi+ instrument. During the measurement charge compensation system was applied. The X-ray source was an aluminum anode with a spot size of 900 μm. For argon cluster sputtering an MAGCIS dual mode ion source was applied working in cluster mode: 6000 eV, 1000 atoms, angle of incidence 45° with respect to the surface normal in a 3 × 3 mm area. This relatively new sputtering technique enables the investigation of organics and soft materials along the depth while minimizing chemical bond damage [27,28]. The samples were fixed to the sample holder by double sided carbon tape. Survey spectra were measured in steps of 0.5 eV with 10 ms dwell time per data point. Silicon (2p), carbon (1s), nitrogen (1s), oxygen (1s), bromine (3d) high-resolution spectra were measured within the spectral range of interest. The data were evaluated in CasaXPS software. The atomic compositions were calculated from the peak areas using sensitivity factors (Althermo-1) after removing the background. The binding energy was set by fixing the C–(C,H) component of the C (1s) peak at 284.8 eV.

The C (1s) peak could be decomposed to 4 components (Lorentzian Asymmetric Lineshape): at 284.8 eV, typical of carbon only bound to carbon and hydrogen; near 286.3 eV, typical of carbon making a single bond with oxygen or nitrogen; near 287.8 eV typical of acetal and amide; near 288.8 eV typical of carboxyl group [29]. The N (1s) peak could be decomposed to three components (Gaussian-Lorentzian functions): near 399.3 eV typical of amine group; near 400.2 eV typical of amide group, the highest binding energy peak near 402 eV can be attributed to protonated (or quaternary) nitrogen [30,31]. Examples for the peak decomposition for carbon and nitrogen are shown in Fig. S6 in Appendix.

2.9. X-ray diffraction measurements

To study the structure and crystallinity of the CS-CTAB samples, X-ray diffraction measurements were performed with an X'pert Pro MPD (Malvern PANalytical B.v., Almelo, Netherlands) device equipped with X'celerator detector and a Cu K-α radiation source (λ = 1.54 Å), operating at 40 kV and 30 mA. The diffractograms were recorded in continuous scanning mode in the scattering range of 4–44° with 0.5° grazing incidence angle, a step size of 0.0167° and 45 s integration time for the coatings on glass substrate and with 10 s integration time for the casted films.

2.10. NMR spectroscopy

Solid-state magic angle spinning (MAS) NMR measurements were carried out on a Varian NMR System 400 MHz spectrometer. For each measurement a Chemomagnetics 4.0 mm narrow-bore double resonance probe was used with a 4 mm standard wall zirconia rotor. The samples were spun at 10 kHz frequency, and the temperature was 20 °C during all measurement. Adamantane was used as an external reference (with chemical shift of 37.77 and 28.74 ppm) in ^{13}C experiments. For the ^{13}C cross polarisation (CP) experiments the following parameters were applied: 2.6 μs pulse length, 10 s recycle delay, 1000 scans and SPINAL-64 ^{1}H decoupling. The contact time for the CP-MAS measurements varied between 20 and 5000 μs.

2.11. Assessment of the antibacterial effect

Two methods were employed to evaluate the antibacterial activity of the coatings. First, a high throughput turbidimetric assay was performed by measuring the optical density (OD) of bacterial suspensions at 630 nm. In parallel, bacterial metabolic activity and viability were assessed

using a colorimetric MTT assay. *Bacillus subtilis* (ATCC 6633) strain was cultured and maintained on agar slant cultures in the laboratory using Luria–Bertani (LB) medium (Thermo Fisher Scientific Inc., USA). For the experiments, a 16 h old (overnight) shaken cell culture was prepared by inoculating one loopful of colony into 30 mL LB broth, and the culture was shaken in the dark at 30 °C, 160 rpm.

To assess the antibacterial effect of the coatings, the coated glass slides were sterilized by autoclaving and then placed into sterile test tubes. An uncoated glass slide was used as a negative control. 6 mL of *B. subtilis* suspension (OD_{600} = 0.1) was added to each tube, and the suspension was incubated for 6 and 24 h. During the experiment samples were shaken at 360 rpm and kept in the dark at 30 °C. Optical density was measured immediately after assembling the test tubes and again following the incubation periods. For the measurement, 200 μL homogeneous samples from the tubes were introduced into the wells of a sterile 96-well polystyrene microplate and the OD was measured at 630 nm, using the DIALAB ELISA EL800 Microplate Reader (Dialab GmbH, Austria).

After the incubation and the OD measurement, 30 μL of 1 mg/mL MTT solution was added to the wells. Then, the microplate was incubated for 15 min at room temperature in the dark, and the absorbance was measured at 544 nm with a Fluostar Optima (BMG Labtech, Germany) microplate reader.

2.12. Statistical analysis

Statistical analysis of the data was performed using mean with standard deviation and ANOVA ($p < 0.05$) tests in OriginPro 2018 software (OriginLab Corporation, Northampton, MA, USA). Significant differences in the tables and figures are marked with lowercase letters, where the different letters mean significantly different data points (Compact Letter Display).

3. Results and discussion

3.1. Surface tension of the precursor solutions

To study the surface accumulation of CS and CTAB in aqueous phase, the surface tension of CTAB solutions and 1% CS-containing CTAB solutions were measured with the pendant drop method. The surface tension values of the two systems are summarized in Fig. 1.

For the pure CTAB solutions (black squares in Fig. 1) a steeply decreasing section can be observed at low concentrations, indicating the interfacial accumulation of CTAB, followed by a breakpoint where surface tension becomes nearly constant, which can be associated with the formation of CTAB micelles. By plotting the data on a semi-logarithmic scale and then fitting straight lines to the linear segments, the CMC value of the surfactant can be determined (see Fig. S3 in Appendix). This value is 0.91 mM which shows good agreement with the CMC value of pure CTAB reported in the literature [32,33].

In the case of CS-containing solutions (red circles in Fig. 1) the surface tension of pure CS solution is lower than that of ultrapure water due to the weak surface activity of the polymer [34]. With increasing CTAB concentration, the surface tension decreases, but more steeply than in the case of pure CTAB solutions, and the breakpoint indicating the CMC is also found at a lower concentration (at 0.29 mM, see Fig. S3 in Appendix). Both observations confirm that the presence of dissolved CS and AcOH increases the surface activity of the surfactant, presumably due to the effect of the counterions, which screen the electrostatic repulsion between the positive head groups of CTA^+ ions in the case of individual molecules, or in the outer layer of micelles. Qazi et al. showed similar changes in the surface tension curves of CTAB solutions in the presence of 5 mM NaCl [33].

3.2. Composition and structure of the coatings

3.2.1. Thickness and refractive index: UV–visible spectroscopy

To study the thickness and the optical properties of the coatings, transmittance spectra were recorded in the 350–1050 nm wavelength range. Representative spectra for the studied systems are shown in Fig. 2 (along with the spectrum of the bare glass substrate).

It can be observed from the spectra that with the increasing CTAB concentration of the precursor solution, the transmittance decreases more significantly in the short wavelength range (presumably due to the light scattering of the coatings), especially in the case of the Gls/CS(1.5 mM) and Gls/CS(3.0 mM) samples. The light scattering can originate from the CTAB crystallites formed during the drying of the coating (see Section 3.2.2). At low surfactant concentrations, when the scattering is not significant, the Hild-model can be used to determine the thickness and refractive index of the coatings based on the transmittance spectra. The fitted values are summarized in Table 1, which show that the thickness and refractive index of the coatings are increasing with

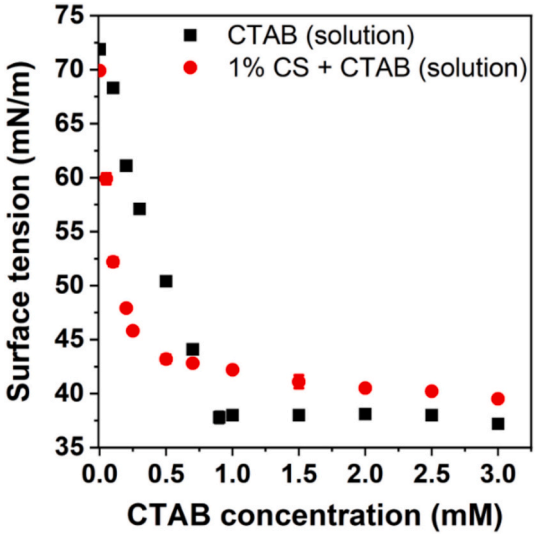

Fig. 1. Surface tension values of pure (black) and 1% CS-containing (red) CTAB solutions (mean ± standard deviation, $n = 10$, the standard deviation is often so small that the markers cover it). (For interpretation of the references to color in this figure legend, the reader is referred to the web version of this article.)

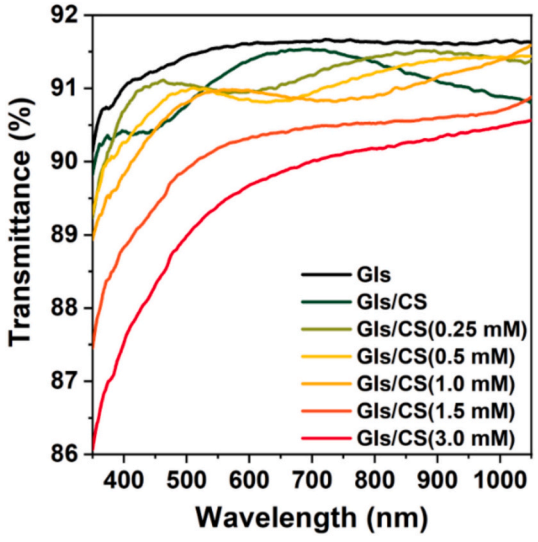

Fig. 2. Transmittance spectra of the nanocoatings made from CS solutions containing CTAB in different concentrations (green-red) and the bare glass substrate (black). (For interpretation of the references to color in this figure legend, the reader is referred to the web version of this article.)

Table 1
Fitted thickness and refractive index values for the coatings made from precursor solutions with low CTAB-content according to the Hild-model. (Mean ± standard deviation, $n = 6$, letters indicate Tukey post hoc groupings following one-way ANOVA; groups not sharing a common letter differ significantly from each other, Tukey-adjusted $p < 0.05$. Full statistical details, including F values, exact p values, and effect sizes η^2, are provided in Table S1 in Appendix.)

Sample	Thickness (nm)	Refractive index (–)
Gls/CS	222 ± 6^{b}	1.5328 ± 0.0026^{b}
Gls/CS(0.25 mM)	281 ± 12^{a}	1.5311 ± 0.0019^{b}
Gls/CS(0.5 mM)	295 ± 17^{a}	1.5380 ± 0.0032^{a}

increasing CTAB concentration.

The change in coating thickness can be interpreted using the Landau-Levich equation, which gives the thickness of the liquid film adhering to the substrate during dip-coating as a function of the parameters of the precursor solution (Eq. (3)).

$$d = 0.94\frac{(u\eta)^{2/3}}{\gamma^{1/6}(\varrho g)^{1/2}} \tag{3}$$

where u is the withdrawal speed, η, ρ, and γ are the dynamic viscosity, density, and surface tension of the precursor solution respectively, and g is the gravitational acceleration. With increasing CTAB concentration, the surface tension decreases (Fig. 1), and – according to the results of Kjoniksen et al. – the viscosity also decreases due to the screening effect of the Br^- ions of CTAB (which reduce the hydrodynamic radius of the CS molecule) [35]. The above two effects influence the thickness of the liquid film during dip-coating; however, the final thickness can also be influenced by the physical structure or the equilibrium water content of the coating, the result of which appears in Table 1.

3.2.2. Crystal structure: X-ray diffraction studies

To study the crystal structure of the coatings and possible interactions between the CS and CTAB, X-Ray diffractograms were recorded of the casted films and coatings. The diffractograms of the films are summarized in Fig. 3. which also includes the data of the pure CTAB powder. The dark green curve (bottom) is typical of CS films and shows good agreement with the diffractogram of a film cast from acetic acid-containing CS solution reported by Eulálio et al. The two peaks at smaller angles (8.6° and 11.8°), which do not appear in the diffractogram of the pure CS powder (see Fig. S4 in Appendix), correspond to the recrystallized structure formed during film casting [36].

Fig. 3 shows that the diffraction peaks of CTAB with the highest intensity (at 7.0°, 17.3°, 20.8°, 21.7° and 38.3°) appear with increasing intensity in the diffraction pattern of the CS(1.5 mM) and CS(3.0 mM) samples. The increase in intensity and the unchanged peak positions (no shift is observed in the case of the mixed samples compared to the characteristic peaks of either CS or CTAB, see the lines in Fig. 3) suggest that in these systems CTAB and CS crystallize in separate phases. Garlea et al. also demonstrated similar XRD patterns and discrete CTAB crystals in CS-CTAB cast films at high CTAB concentrations (above 6 mM) [37,38]. In the XRD patterns of the nanocoatings applied to glass (see Fig. S5 in Appendix), a sharp diffraction peak around 7° can be observed only in the case of the Gls/CS(3.0 mM) sample, which may correspond to the peak of CTAB at the same diffraction angle, and thus may prove that CTAB crystals can also form during the drying of nanocoatings at sufficiently high surfactant concentrations. Using the Scherrer equation [39,40], the average crystallite size can be determined from the parameters of this peak, and is found to be approximately 63 nm (for detailed calculation, see Section S3.1 in Appendix). These crystals can be responsible for the increased light scattering of the coatings (see Fig. 2).

3.2.3. NMR spectroscopy

Solid-state ^{13}C CP-MAS NMR spectra of the casted CS-CTAB films and crystalline CTAB were recorded to study the molecular interactions and

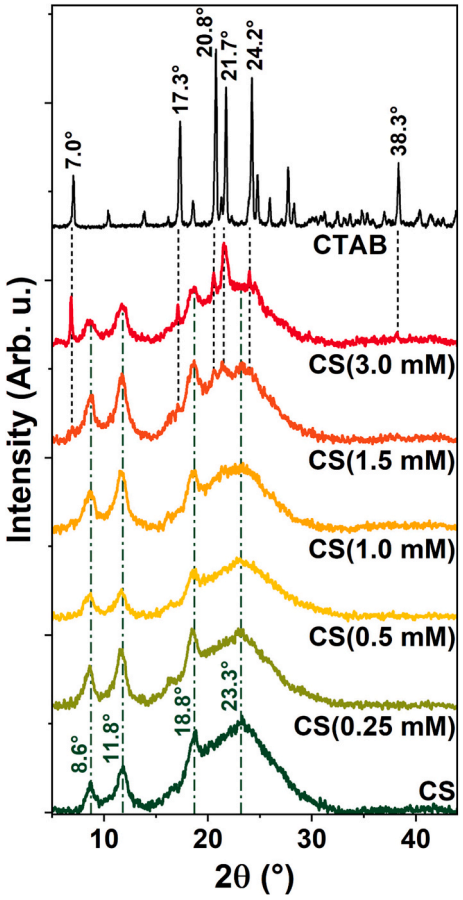

Fig. 3. X-ray diffraction patterns of the casted CS-CTAB films made from CS solutions containing CTAB in different concentrations (green-red) and pure CTAB (black), with the diffraction angle values of the peaks with highest intensity. (For interpretation of the references to color in this figure legend, the reader is referred to the web version of this article.)

structure of the CS-CTAB systems. The ^{13}C NMR spectra are summarized in Fig. 4. The dark green spectrum (bottom) shows characteristic peaks of CS and AcOH, the identification of which is shown in the inset image and was based on the study by Facchinatto et al. [41]. The black spectrum (top) is typical for crystalline CTAB, where the most intense peak can be attributed to the methylene carbon atoms of the carbon chain of the CTA^+ ion around 32 ppm (the peaks were identified based on the study of Lavine et al. [42]).

In the case of the CS-CTAB samples (light green-red), the characteristic peaks of CS and AcOH are clearly visible, however, from the characteristic peaks of CTAB, only the signal of the methylene carbon atoms is observed, since the intensity of the other peaks is significantly lower. A closer look at the spectra (Fig. S7 in Appendix) shows that between 28 and 33 ppm two peaks appear: a more intense peak at 30 ppm, which is visible even at the lowest CTAB content, and a lower intensity peak at 32 ppm. According to the results of Xu et al., the peak at 32 ppm belongs to crystalline CTAB (as is the position of the peak in the spectrum of the pure surfactant), while the peak at 30 ppm is characteristic of CTAB solution, thus indicating the presence of individual CTAB molecules or micelles [43]. The difference is presumably due to the different mobility of the methylene groups forming the carbon chains of CTA^+ ions in the crystalline and individual molecular or micellar states. This is also confirmed by the CP-MAS build-up curves of the C_c carbons, which are summarized in Fig. S8 in the Appendix. In the case of the CS(3.0 mM) sample, the normalized build-up curve corresponding to the 32 ppm peak is close to the curve corresponding to the C_c carbon of pure CTAB, and both curves reach their maximum value at

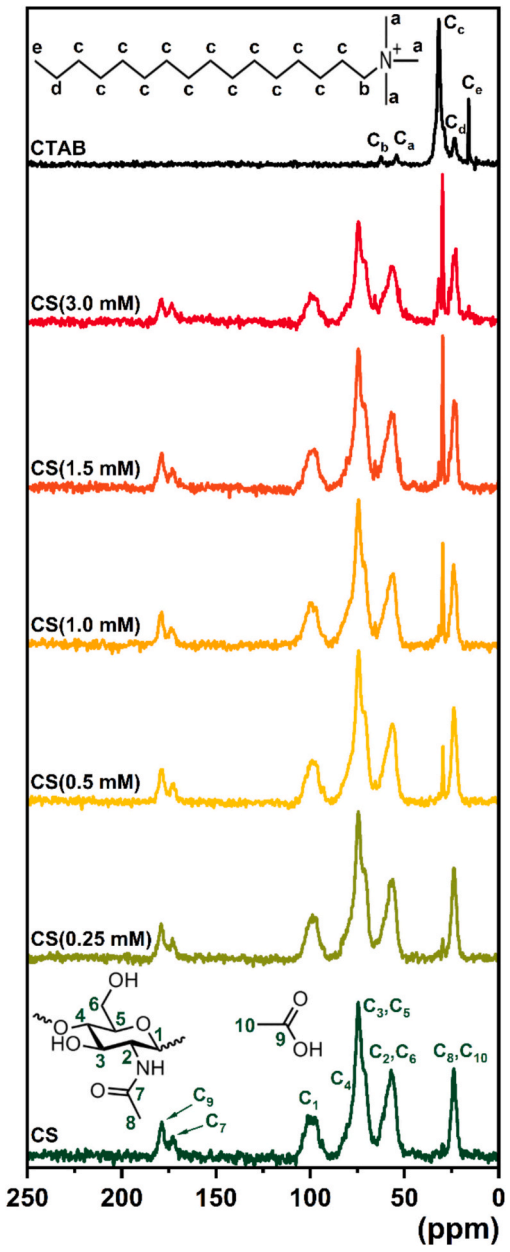

Fig. 4. Solid-state ^{13}C CP-MAS NMR spectra (with 1000 μs contact time) of the casted CS-CTAB films made from CS solutions containing CTAB in different concentrations (green-red) and pure CTAB (black). For the peak notations Ref. [41,42] were used, see the inset pictures. (For interpretation of the references to color in this figure legend, the reader is referred to the web version of this article.)

500 μs contact time. However, the build-up curve corresponding to the 30 ppm peak is different, and its maximum is at 2000 μs indicating different molecular interactions and mobility than that observed for crystalline CTAB. The ratio of the peaks at 30 and 32 ppm for the CS(3.0 mM) sample is approximately 1:1.9, which means that next to the CTAB crystals detected by XRD (see Section 3.2.2) and AFM (see Section 3.3.1), there is also a significant amount (almost twice as much) of individual molecular/micellar CTAB in the coatings.

3.2.4. *In-depth composition: X-ray photoelectron spectroscopy*

To study the accumulation and concentration gradients of CTAB within the coatings, XPS cluster depth profiling was used. During the measurement, an XPS spectrum was recorded, then a thin layer was etched off the surface of the sample with argon cluster sputtering, followed by another measurement, so that the composition of the layer could be measured layer by layer, from the coating surface towards the glass substrate. Complete removal of the coating was indicated by the appearance of the Si (2p) peak in the spectrum (min. 5 At. %), which is only contained in the glass substrate. Since the amount of CTA^+ ions is best characterized by the At. % of aliphatic carbon (C—C, C—H), and quaternary nitrogen (N^+) in the coatings, these were determined based on the decomposition of the peaks of the corresponding elements (by proportioning the peak area of the given sub-peak by the At. % value of the total peak area). These values are summarized in Fig. 5a and b for N and C respectively.

Fig. 5a shows that CTA^+ ions are accumulated at the coating-air interface (0 sputtering time) even at the lowest concentration. As the CTAB concentration increases, the interfacial accumulation becomes increasingly significant, with an almost fivefold increase in the Gls/CS (1.5 mM) sample and an eightfold increase in the Gls/CS(3 mM) sample compared to the bulk phase composition. At these two concentrations, accumulation can be observed not only at the coating-air interface, but also at the coating-glass interface, presumably because of the electrostatic attraction due to the negative surface charge of the glass substrate [44]. In Fig. 5b (aliphatic carbon), these concentration differences and the accumulation at the coating-glass interface (even at lower concentrations, 0.5 and 1 mM) can be observed even better. Similar concentration differences were observed in the case of anionic surfactant-modified CS coatings, where the surfactant was enriched at the coating-air interface, while it was depleted at the coating-glass interface due to electrostatic repulsion from the negatively charged glass surface [34].

Interestingly, for the Gls/CS(3 mM) sample, the surfactant concentration is higher in the middle of the coating than near the interfacial region. Presumably, the diffusion processes leading to surface accumulation during coating formation are slowed by the concentration of the precursor solution during drying, so that CTA^+ ions are unable to reach the interfaces from the full depth of the coating, forming a region richer in surfactant in the middle. This region may serve as a reservoir to replace the surfactant molecules that leave the surface during a potential application (for surface studies regarding this stability, see Section 3.3.2). Fig. 5c shows that the Br^- counterions move together with the CTA^+ ions, thus an accumulation of Br^- ions can also be observed at the coating-air and coating-glass interfaces of the nanolayers.

Assuming that the thickness of the coatings decreases by the same amount in each Ar-cluster etching cycle during the measurement, the thickness of the interfacial region in Fig. 5 can be estimated by dividing the known thickness of the coatings (see Table 1) by the number of cycles. This value stays under 10 nm up to the Gls/CS(1.0 mM) sample and is estimated to be more than 50 nm for the Gls/CS(3.0 mM) sample.

3.3. *Surface properties of the coatings*

3.3.1. *Surface morphology*

To study the surface morphology of the coatings, AFM images were taken from the Gls/CS, Gls/CS(0.25 mM), Gls/CS(1.0 mM) and Gls/CS (3.0 mM) samples in 5 × 5 μm areas. The height and phase images for these samples are summarized in Fig. 6.

The images show that the surface of the Gls/CS sample is smooth and homogeneous with a few protrusions of approximately 10 nm (Fig. 6a). In the case of the Gls/CS(0.25 mM) sample, the surface is smooth (Fig. 6b), but the pattern appearing in the phase image (Fig. 6f) suggests that there are fluctuations in the surface composition, which presumably indicates the appearance of CS-CTAB associates (the pattern can be better observed in Fig. S9 in the Appendix). This fluctuation pattern (which is typical of spinodal decomposition [45]) is even more visible in the case of the Gls/CS(1.0 mM) sample, especially in the height image (Fig. 6c), while in the case of the Gls/CS(3.0 mM) sample, complete phase separation occurs; the roughness of the coating increases (see the

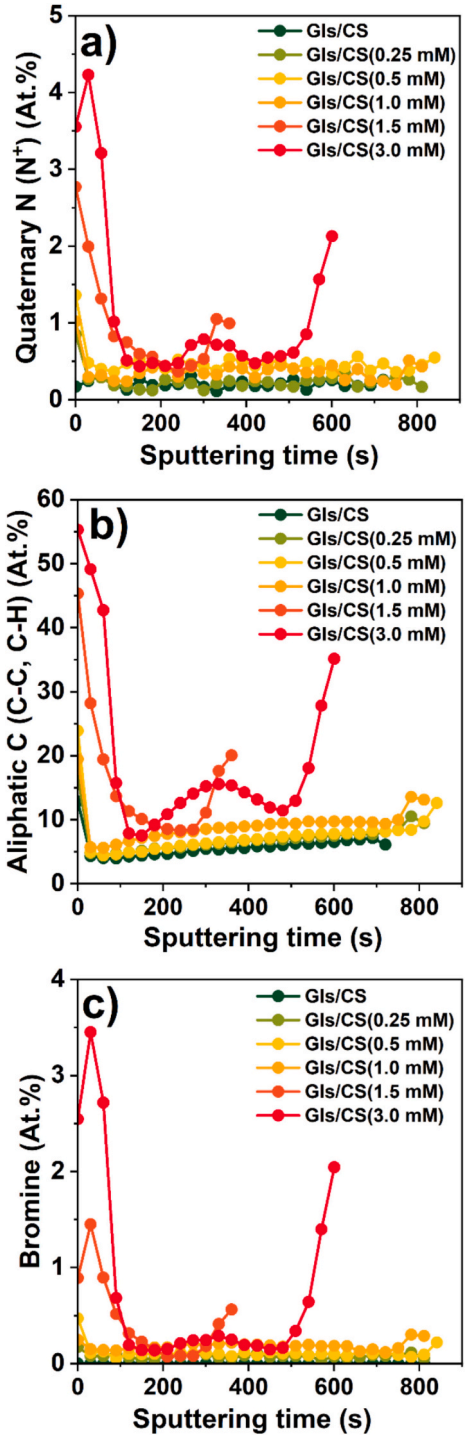

Fig. 5. In-depth composition of the CTAB-containing CS coatings on glass substrate. The distribution of quaternary nitrogen (a) and aliphatic carbon (b) in the coating indicates the accumulation of CTA^+ ions, while the amount of bromine (c) indicates the accumulation of Br^- ions. The end of the data points indicates the reaching of the glass substrate (determined by the appearance of the Si (2p) peak), the difference in the sputtering times thus far is due to the different thickness and composition of the coatings.

range of the z-scale) and CTAB crystals appear in the coating as confirmed by previous XRD and NMR results. These crystals were also visible on the AFM images of the previously mentioned articles by Garlea et al. [37,38]. The Wenzel surface roughness factors (ratios between the actual and projected surface area) were below 1.008 in all cases (determined in 20 × 20 μm areas, see Fig. S10 in Appendix).

3.3.2. *Wettability and surface free energy*

To calculate the surface free energy of the coatings and investigate the effect of CTAB on the surface properties, contact angle measurements were performed with ultrapure water, diiodomethane and formamide. From the advancing contact angles the total surface free energy and its components were calculated according to the van Oss model. The advancing contact angles of the three liquids on the different nanocoatings are summarized in Fig. 7a, while the calculated surface free energy components are in Fig. 7b (Lifshitz–van der Waals and acid–base component) and Fig. 7c (electron acceptor and electron donor components).

Based on the advancing water contact angles shown in Fig. 7a, it can be concluded that the surface of the coatings became more hydrophilic upon the addition of CTAB (the advancing water contact angle decreased from 70° to approximately 30°). Since the XPS studies revealed that CTAB is accumulated at the coating-air interface (see Section 3.2.4), the decrease in the contact angle can be explained multiple ways. The molecular CTAB or the CTAB crystals in the interfacial layer can increase the surface roughness of the coating, which – according to the Wenzel model – results in a better wettability (decrease of apparent contact angles) [46]. However, considering the small roughness values (see Section 3.3.1) this effect is not significant. Another explanation can be the dissolution of CTAB from the coating into the water droplet used for contact angle determination, lowering its surface tension, therefore decreasing the contact angle. However, this effect also cannot be significant in the case of the coatings up to the Gls/CS(1.0 mM) sample, therefore the underlying effect must be something else. For detailed calculations and justification see Section S3.2 in Appendix.

Nevertheless, CTA^+ ions accumulated at the coating-air interface can be oriented in such a way that the positively charged head groups point towards the air. Although the reverse orientation is common for surfactants (nonpolar chain in the vapor phase, polar head group in the coating) [34], the hydrophobic interactions that dominate in solution can form polymer-surfactant associates in which the head groups are oriented outwards (bottle brush structure) [16]. If this structure is maintained during the drying of the coating, an interfacial layer can be formed in which the cationic head groups are oriented towards the air, making the surface more polar. This effect can be produced even by a single layer of CTA^+ ions (independent surface action [47,48]), which explains why it is observed at the lowest CTAB concentration (0.25 mM) and why it does not change with increasing concentration (up to 1 mM). We assume that this explanation correctly describes the structure of the coating surface, since it is most consistent with the measurement results.

This explanation is further confirmed by the values of the surface free energy components (Fig. 7b). In the presence of CTAB, the value of γ^{LW} decreases and the value of γ^{AB} increases compared to the pure CS coating, which means that the non-polar nature of the surface decreases, while its polar nature increases (the CTA^+ and Br^- ions can mask the non-polar groups of CS). Such "masking effect" was observed previously for non-polar side chains in the case of decanoic acid modified CS nanocoatings [49].

Based on Fig. 7c, the increase in γ^{AB} is primarily due to the increase in the Lewis-basic component (γ^-). In the case of the Gls/CS sample, the γ^- component is also the determining one (presumably due to the Lewis-basic nature of the surface amino groups), however, the addition of CTAB further increases the number of electron-donor groups on the surface. This is an interesting observation, since the head group of the CTA^+ ion is positively charged, but Janczuk et al. also found that the value of the electron donor component (γ^-) is higher for CTAB-coated surfaces (although they do not provide an explanation) [50]. Our assumption is that since the quaternary ammonium group does not have strong Lewis acidic or strong Lewis basic character [51], the surface properties are influenced by the Br^- ion, which is also accumulated on the surface (see Fig. 5c), and has an electron donor character, which causes the increase of γ^-.

To investigate the aqueous stability of the coating surface and the

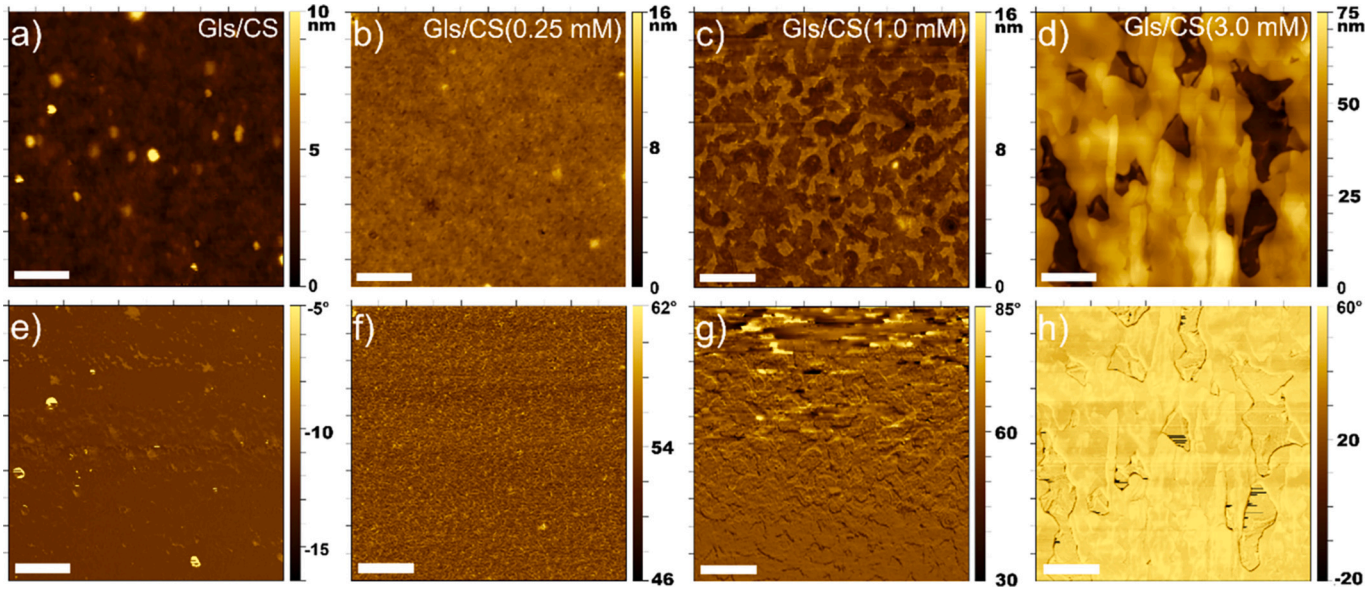

Fig. 6. Height (a–d) and phase (e–h) images for nanocoatings on glass substrate made from precursor solutions containing different amounts of CTAB. The side length of images is 5 μm, scale bars are 1 μm.

"reservoir effect" mentioned in Section 3.2.4 in case of the damage of the surface CTAB layer, the coatings were soaked in ultrapure water for 10 min, dried under ambient conditions, then additional water contact angle measurements were performed. The results (advancing water contact angles on the as-prepared and soaked coatings) are summarized in Fig. S11 in Appendix. While in the case of the Gls/CS sample there is no difference between the contact angles measured before and after soaking, in the case of the systems containing CTAB, the contact angle value increased in all cases. The extent of the increase is the largest in the case of the Gls/CS(0.25 mM) coating (after soaking the contact angle approaches those measured in the case of the Gls/CS coatings), which suggests that CTAB has been desorbed or dissolved from the surface. However, in the case of samples above 1 mM CTAB concentration the extent of the increase is smaller, the contact angles are around 35°; the surface of the coatings is still hydrophilic. Presumably, during soaking in the ca. pH neutral ultrapure water and drying, a new equilibrium composition and structure is formed on the surface of the coatings, which still contains a sufficient amount of CTAB. These surface properties that remain even under the harsh conditions of aqueous soaking (despite the possible partial desorption or dissolution of CTAB) demonstrate the aqueous stability of the coatings.

3.3.3. Surface zeta potential

To demonstrate the orientation of the CTA^+ ions with their head groups towards the air and thus the increase in the surface charge density of the coatings, surface zeta potential (SZP) measurements were performed in aqueous medium (pH = 6 AcOH-NaAc buffer) using aminated SiO_2 tracer particles (Size: 0.234 ± 0.01 μm; NH_2 > 30 μmol/g). The SZP values of the nanocoatings on glass substrates are shown in Fig. 8.

The SZP measured for the Gls/CS coating (ca. 22 mV) is presumably due to the protonated amino groups located on the surface of the coating. Zhang and Bai measured a similar positive SZP value for CS coatings at pH 6 [52]. Upon addition of CTAB, the SZP takes on a more positive value (above 30 mV), indicating an increase in the cationic charge density of the surface. This is presumably due to the above-mentioned oriented accumulation of CTA^+ ions, and the phenomenon that CTA^+ ions are quasi attached to the coating by hydrophobic interactions, while Br^- ions can dissociate from the surface into the aqueous medium, leaving behind a surface with a positive charge density. The measured SZP values for CTAB monolayers formed on hydrophobic surfaces (graphite or activated carbon) with the head groups oriented outwards are between +40 and +70 mV [53,54]. Since on the surface of the Gls/CS(3.0 mM) sample the CTAB monolayer is presumably not perfect due to the irregular structure of the associates, the slightly lower SZP value is appropriate.

3.3.4. Possible surface structure of the coatings

Based on the above results, Fig. 9 shows the possible structure of the interfacial layer of the coatings in three representative cases: without CTAB, with a small amount of CTAB (no crystals) and with a large amount of CTAB (after phase separation). Without CTAB, only the CS chains appear on the surface, causing a slight positive charge density (see Fig. 8). Even with the addition of a small amount of surfactant, CTAB molecules appear on the surface, making it more polar (see Fig. 7 and its interpretation), while micellar structures may form in the bulk due to the increase in concentration during the drying of the solution [18]. Above 1 mM CTAB concentration, CTAB crystals form, further increasing the cationic nature of the surface (Fig. 8). These crystals are visible in the AFM image of Fig. 6d as well. Note, that the structures in the figure form only in the interfacial layer of the coating (based on the XPS results, Fig. 5), the amount of CTAB in the bulk of the coating is much lower.

3.3.5. Antimicrobial effect of the coatings

Turbidimetric and colorimetric assays were used to estimate the antibacterial activity of the coatings against a Gram-positive bacterium *Bacillus subtilis*. It is an excellent indicator organism for evaluating antibacterial coatings and biomaterials, possesses a thick peptidoglycan layer enriched with negatively charged teichoic and lipoteichoic acids, making the bacterial surface highly responsive to cationic antimicrobial compounds such as CTAB and CS [55,56]. The results of the measurements are summarized in Fig. 10, in which the filled markers indicate the results of CS-CTAB coatings on glass substrate, while the empty markers indicate the results of the control samples (clean glass substrates).

Based on the results, all CS-CTAB coatings exhibited significant antibacterial activity against *B. subtilis* by demonstrating more than 80% inhibition at all investigated time points in both assays. The only exception was the Gls/CS(0.25 mM) coating, which inhibited bacterial growth and viability by approximately 67% and 80% after 6 h of incubation compared to the untreated control, but the antibacterial effect

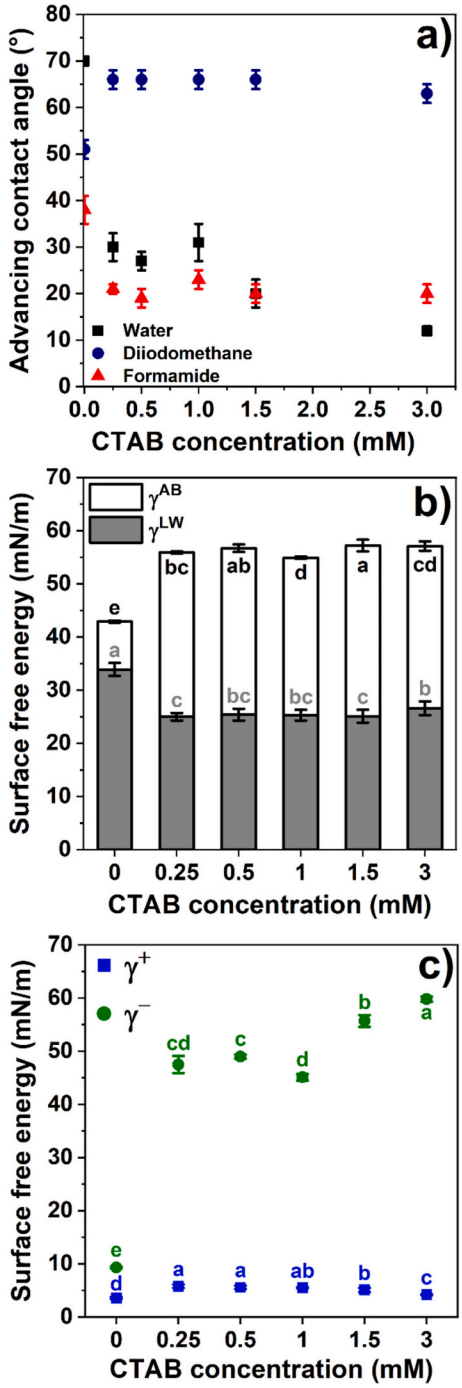

Fig. 7. Advancing contact angles of the measuring liquids on the surface of the nanocoatings on glass (a) and the calculated surface free energy components according to the van Oss model (Lifshitz–van der Waals γ^{LW}, and acid–base γ^{AB} component) (b) and electron acceptor γ^{+}, and electron donor γ^{-}, components (c). (Mean ± standard deviation, $n = 12$, letters indicate Tukey post hoc groupings following one-way ANOVA; groups not sharing a common letter differ significantly from each other, Tukey-adjusted $p < 0.05$. Full statistical details, including F values, exact p values, and effect sizes η^2, are provided in Table S1 in Appendix.)

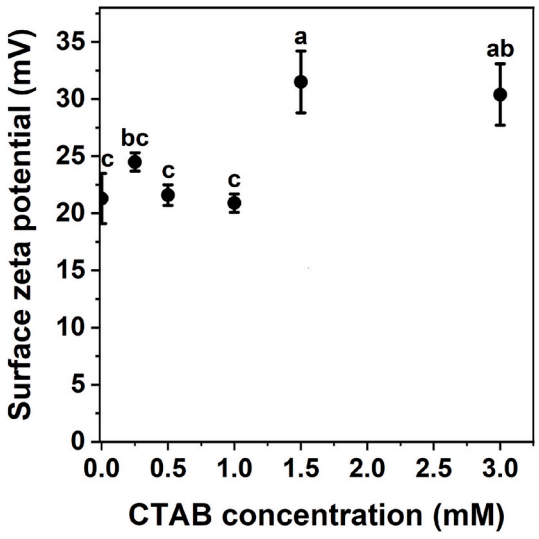

Fig. 8. Surface zeta potential values of nanocoatings on glass substrate made from CS-CTAB precursor solutions with different CTAB concentrations. (Mean ± standard deviation, $n = 3$, letters indicate Tukey post hoc groupings following one-way ANOVA; groups not sharing a common letter differ significantly from each other, Tukey-adjusted $p < 0.05$. Full statistical details, including F values, exact p values, and effect sizes η^2, are provided in Table S1 in Appendix.)

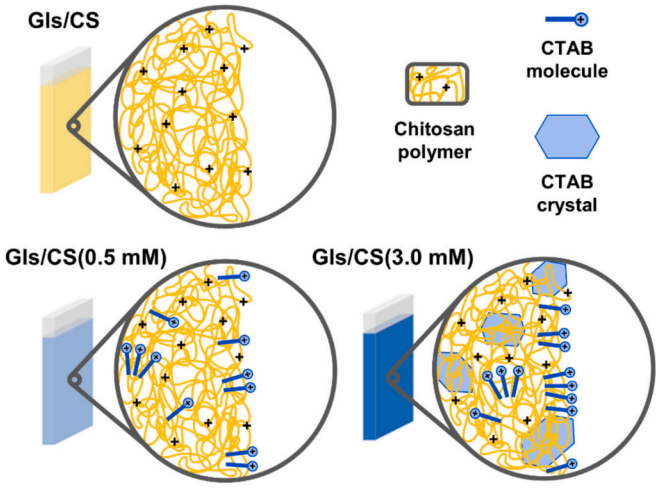

Fig. 9. Schematic structure of some selected coatings representing the interfacial layer in the case of no CTAB (Gls/CS), low CTAB content (Gls/CS(0.5 mM)) and high CTAB content (Gls/CS(3.0 mM)).

decreased after 24 h of incubation, showing approximately 10% inhibition, as determined by both assays, (although the effect remained statistically significant). There are several factors that may contribute to this phenomenon. The lower concentration of CTAB may not have been sufficient to maintain prolonged membrane disruption during extended bacterial exposure. The partial depletion or rearrangement of CTAB molecules from the coating interface over time (see the soaking experiments in Section 3.3.2) may also have reduced antimicrobial accessibility. Lastly, surviving bacterial populations may have adapted to sublethal CTAB concentrations through physiological stress responses or biofilm-associated protection mechanisms (as it was reported previously by Buffet-Bataillon et al. [57]).

However, in the case of samples with higher CTAB content, a significant antibacterial effect was measured, which was consistent with previous reports describing the strong bactericidal activity of CTAB-containing systems [58,59]. Although the antibacterial effect may result from CTAB molecules possibly dissolved (release-killing) or remaining on the surface of the coating (contact-killing), the maintenance of this strong antibacterial effect against *B. subtilis* after prolonged incubation (24 h) suggests that the system remained sufficiently bioactive to interact with bacterial cells. Future investigations are needed to distinguish the effects of release- and contact-killing mechanisms, and to

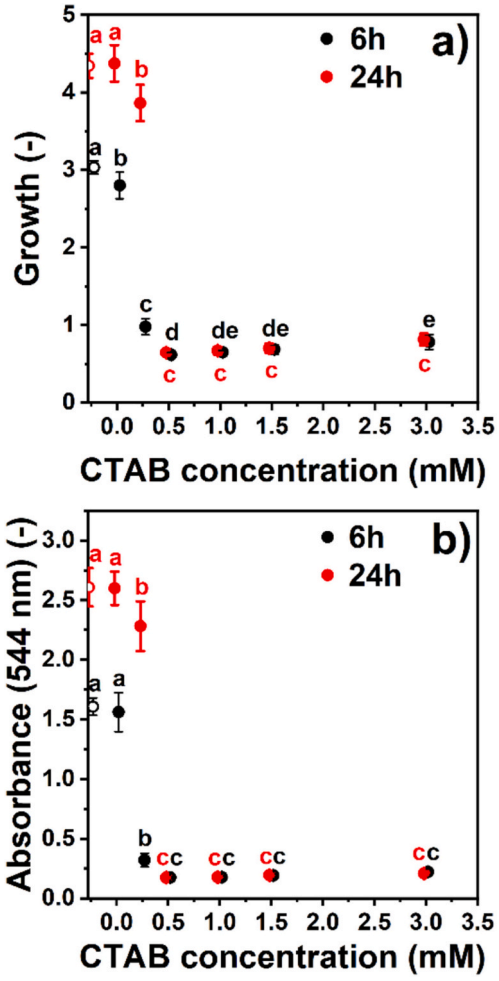

Fig. 10. Effect of the CS-CTAB nanocoatings on the growth of *B. subtilis* after 6 and 24 h of incubation (a) and viability of *B. subtilis* in the presence of CS-CTAB nanocoatings after 6 and 24 h of incubation (b). (Mean ± standard deviation, $n = 6$, letters indicate Tukey post hoc groupings following one-way ANOVA; groups not sharing a common letter differ significantly from each other, Tukey-adjusted $p < 0.05$. Full statistical details, including F values, exact p values, and effect sizes η^2, are provided in Table S1 in Appendix.)

evaluate the effectiveness of the coatings against additional Gram-positive and Gram-negative pathogens (e.g. *Staphylococcus aureus*), including clinically relevant multidrug-resistant strains.

4. Conclusions

Chitosan-based nanocoatings with enhanced cationic character were fabricated via interfacial self-assembly of CTAB. Films were deposited onto glass substrates from aqueous solutions of 1% chitosan and 0–3.0 mM CTAB. At low concentrations (<1.0 mM), homogeneous 200–300 nm thick layers formed, whereas higher surfactant contents induced phase separation and the formation of CTAB crystallites, as confirmed by X-ray diffraction, solid-state NMR, and AFM.

XPS depth profiling revealed CTAB accumulation at the coating-air interface. Synergistic polymer-surfactant interactions promote a preferential molecular orientation with cationic head groups facing the air, amplifying the cationic character of the surface and enhancing its antibacterial effect against *B. subtilis* bacteria. Depth profiles also identified a surfactant-rich bulk region, suggesting a quasi-self-healing mechanism whereby CTAB molecules from this internal reservoir can replace surfactant molecules depleted or desorbed during application. These robust surfaces represent a promising strategy for antimicrobial coatings requiring sustained interfacial bioactivity.

CRediT authorship contribution statement

Péter Márton: Writing – original draft, Visualization, Methodology, Investigation, Formal analysis, Conceptualization. **Petra Demény:** Writing – original draft, Resources, Methodology, Investigation, Formal analysis. **Adél Rácz:** Writing – review & editing, Validation, Resources, Investigation, Formal analysis. **Tamás Szabó:** Writing – review & editing, Validation, Resources, Investigation, Formal analysis. **Zsófia Keresztes:** Writing – review & editing, Validation, Resources. **Bence Balterer:** Writing – review & editing, Validation, Resources, Investigation, Formal analysis. **János Madarász:** Writing – review & editing, Validation, Resources, Investigation, Formal analysis. **Norbert Nagy:** Writing – review & editing, Validation, Resources, Investigation, Formal analysis. **Rita Márton:** Writing – review & editing, Validation, Resources, Formal analysis. **Mónika Molnár:** Writing – review & editing, Validation, Resources, Formal analysis. **Zoltán Hórvölgyi:** Writing – review & editing, Supervision, Project administration, Methodology, Funding acquisition, Conceptualization.

Declaration of competing interest

The authors declare that they have no known competing financial interests or personal relationships that could have appeared to influence the work reported in this paper.

Acknowledgments

The authors are thankful to Izabella Kertész for the sample preparation and preliminary experiments as well as Benjámin Gyarmati and Bence Mihalovics from the Soft Matters Group of Budapest University of Technology and Economics for the viscosity measurements and molecular weight determination. The authors are grateful to Borbála Tegze for proofreading the manuscript. Projects no. TKP-9-8/PALY-2021 and TKP-6-6/PALY-2021 have been implemented with the support provided by the Ministry of Culture and Innovation of Hungary from the National Research, Development and Innovation Fund, financed under the TKP2021-EGA and TKP2021-NVA funding schemes. Further support was provided by the National Research Development and Innovation Office (Project no.: EKÖP-25-4-1-BME-132 and STARTING 152904). The project was supported by the Doctoral Excellence Fellowship Programme (DCEP, grant no.: DKÖP-26-1-BME-115) is funded by the National Research Development and Innovation Office of the Ministry of Culture and Innovation and the Budapest University of Technology and Economics.

Appendix A. Supplementary data

Supplementary data to this article can be found online at https://doi.org/10.1016/j.ijbiomac.2026.153416.

Data availability

Data will be made available on request.

References

[1] Á.F. Szőke, G.S. Szabó, Z. Hórvölgyi, E. Albert, A.G. Végh, L. Zimányi, L. M. Muresan, Accumulation of 2-acetylamino-5-mercapto-1,3,4-thiadiazole in chitosan coatings for improved anticorrosive effect on zinc, Int. J. Biol. Macromol. 142 (2020) 423–431, https://doi.org/10.1016/j.ijbiomac.2019.09.114.
[2] M. Bertrand, S. Simonin, B. Bach, Applications of chitosan in the agri-food sector: a review, Carbohydr. Res. 543 (2024) 109219, https://doi.org/10.1016/j.carres.2024.109219.
[3] F.S. Rezaei, F. Sharifianjazi, A. Esmaeilkhanian, E. Salehi, Chitosan films and scaffolds for regenerative medicine applications: a review, Carbohydr. Polym. 273 (2021) 118631, https://doi.org/10.1016/j.carbpol.2021.118631.

[4] M. Dabóczi, E. Albert, E. Agócs, M. Kabai-Faix, Z. Hórvölgyi, Bilayered (silica–chitosan) coatings for studying dye release in aqueous media: the role of chitosan properties, Carbohydr. Polym. 136 (2016) 137–145, https://doi.org/10.1016/j.carbpol.2015.09.025.

[5] F.M. Shannan ALzahrani, S.M. Albukhari, H. Alwael, Z. Zaheer, Chitosan stability in acetic acid-permanganate solutions: spectroscopic and viscometric approach, Int. J. Biol. Macromol. 320 (2025) 145786, https://doi.org/10.1016/j.ijbiomac.2025.145786.

[6] S. Shankar, S. Joshi, R.K. Srivastava, A review on heavy metal biosorption utilizing modified chitosan, Environ. Monit. Assess. 195 (2023) 1350, https://doi.org/10.1007/s10661-023-11963-7.

[7] Z. Zaheer, Chitosan-capped silver nanoparticles: fabrication, oxidative dissolution, sensing properties, and antimicrobial activity, J. Polym. Res. 28 (2021) 348, https://doi.org/10.1007/s10965-021-02673-0.

[8] Z. Zaheer, Chitosan capped noble metal doped CeO2 nanomaterial: synthesis, and their enhanced catalytic activities, Int. J. Biol. Macromol. 166 (2021) 1258–1271, https://doi.org/10.1016/j.ijbiomac.2020.11.008.

[9] S.A. Hejazi, Z. Zaheer, S.A. Kosa, Chitosan and cetyltrimethylammonium bromide capped iridium-silver bimetallic nanoparticles: a comparative study, J. Mol. Liq. 358 (2022) 119182, https://doi.org/10.1016/j.molliq.2022.119182.

[10] C. Ardean, C.M. Davidescu, N.S. Nemeş, A. Negrea, M. Ciopec, N. Duteanu, P. Negrea, D. Duda-Seiman, V. Musta, Factors influencing the antibacterial activity of chitosan and chitosan modified by functionalization, Int. J. Mol. Sci. 22 (2021) 7449, https://doi.org/10.3390/ijms22147449.

[11] I.B. Amor, H. Hemmami, S.E. Laouini, A.G. Abdelaziz, A. Barhoum, Influence of chitosan source and degree of deacetylation on antibacterial activity and adsorption of AZO dye from water, Biomass Convers. Biorefinery 14 (2024) 16245–16255, https://doi.org/10.1007/s13399-023-03741-9.

[12] E.M. Hefzy, T.E.E. Radwan, B.M.M. Hozayen, E.E. Mahmoud, M.A.F. Khalil, Antiseptics and mupirocin resistance in clinical, environmental, and colonizing coagulase negative Staphylococcus isolates, Antimicrob. Resist. Infect. Control 12 (2023) 110, https://doi.org/10.1186/s13756-023-01310-3.

[13] R. Chen, C. Qi, Z. Dong, J. Xu, C. Lei, Facile fabrication of hydrophobic paper via cetyltrimethylammonium bromide - modified acrylic copolymer coating for sustainable packaging, Prog. Org. Coat. 209 (2025) 109643, https://doi.org/10.1016/j.porgcoat.2025.109643.

[14] X. Wang, Y. Yin, C. Wang, New approach to impart antibacterial effect and improve ink jet printing properties with modified SiO2 sols containing cationic biocides, Colloids Surf. A Physicochem. Eng. Aspects 361 (2010) 51–55, https://doi.org/10.1016/j.colsurfa.2010.03.007.

[15] G.C. Lainioti, D. Druvari, Designing antibacterial-based quaternary ammonium coatings (surfaces) or films for biomedical applications: recent advances, Int. J. Mol. Sci. 25 (2024) 12264, https://doi.org/10.3390/ijms252212264.

[16] N. Khan, B. Brettmann, Intermolecular interactions in polyelectrolyte and surfactant complexes in solution, Polymers 11 (2019) 51, https://doi.org/10.3390/polym11010051.

[17] F. Schulze-Zachau, B. Braunschweig, C n TAB/polystyrene sulfonate mixtures at air–water interfaces: effects of alkyl chain length on surface activity and charging state, Phys. Chem. Chem. Phys. 21 (2019) 7847–7856, https://doi.org/10.1039/C9CP01107B.

[18] H. Bao, L. Li, H. Zhang, Influence of cetyltrimethylammonium bromide on physicochemical properties and microstructures of chitosan–TPP nanoparticles in aqueous solutions, J. Colloid Interface Sci. 328 (2008) 270–277, https://doi.org/10.1016/j.jcis.2008.09.003.

[19] A. Singh, V. Kumar, S. Anand, D. Phukan, N. Pandey, Fungi-derived Chitosan-CTAB composite-based electrode for electrochemical simultaneous detection of Cd (II) and Pb (II), Int. J. Biol. Macromol. 280 (2024) 136113, https://doi.org/10.1016/j.ijbiomac.2024.136113.

[20] W. Loh, C. Brinatti, K.C. Tam, Use of isothermal titration calorimetry to study surfactant aggregation in colloidal systems, Biochim. Biophys. Acta Gen. Subj. 1860 (2016) 999–1016, https://doi.org/10.1016/j.bbagen.2015.10.003.

[21] E. Hild, A. Deák, L. Naszályi, Ö. Sepsi, N. Ábrahám, Z. Hórvölgyi, Use of the optical admittance function and its WKB approximation to simulate and evaluate transmittance spectra of graded-index colloidal films, J. Opt. A Pure Appl. Opt. 9 (2007) 920, https://doi.org/10.1088/1464-4258/9/10/023.

[22] E. Albert, P. Basa, B. Fodor, Z. Keresztes, J. Madarász, P. Márton, D. Olasz, A. S. Rácz, G. Sáfrán, T. Szabó, B. Tegze, T. Höltzl, Z. Hórvölgyi, Experimental and computational synthesis of TiO2 sol–gel coatings, Langmuir 41 (2025) 704–718, https://doi.org/10.1021/acs.langmuir.4c03959.

[23] C.J. Van Oss, M.K. Chaudhury, R.J. Good, Interfacial Lifshitz-van der Waals and polar interactions in macroscopic systems, Chem. Rev. 88 (1988) 927–941, https://doi.org/10.1021/cr00088a006.

[24] I. Mohammed-Ziegler, Z. Hórvölgyi, A. Tóth, W. Forsling, A. Holmgren, Wettability and spectroscopic characterization of silylated wood samples, Polym. Adv. Technol. 17 (2006) 932–939, https://doi.org/10.1002/pat.778.

[25] Gwyddion software. https://gwyddion.net/ (last access: 2026.02.02). (n.d.).

[26] J.C.W. Corbett, F. McNeil-Watson, R.O. Jack, M. Howarth, Measuring surface zeta potential using phase analysis light scattering in a simple dip cell arrangement, Colloids Surf. A Physicochem. Eng. Asp. 396 (2012) 169–176, https://doi.org/10.1016/j.colsurfa.2011.12.065.

[27] A.S. Racz, Atomistic insights into salicylic acid treatment on human keratinized skin by XPS combined with argon gas cluster sputtering: a pilot study, Surf. Interfaces 55 (2024) 105452, https://doi.org/10.1016/j.surfin.2024.105452.

[28] A.S. Racz, M. Menyhard, Evaluation methods for XPS depth profiling; a review, Appl. Surf. Sci. Adv. 30 (2025) 100872, https://doi.org/10.1016/j.apsadv.2025.100872.

[29] J.B.M. Rocha Neto, T.B. Taketa, R.A. Bataglioli, S.B. Pimentel, D.M. Santos, A. Fiamingo, C.A.R. Costa, S.P. Campana-Filho, H.F. Carvalho, M.M. Beppu, Tailored chitosan/hyaluronan coatings for tumor cell adhesion: effects of topography, charge density and surface composition, Appl. Surf. Sci. 486 (2019) 508–518, https://doi.org/10.1016/j.apsusc.2019.04.227.

[30] N. Graf, E. Yegen, T. Gross, A. Lippitz, W. Weigel, S. Krakert, A. Terfort, W.E. S. Unger, XPS and NEXAFS studies of aliphatic and aromatic amine species on functionalized surfaces, Surf. Sci. 603 (2009) 2849–2860, https://doi.org/10.1016/j.susc.2009.07.029.

[31] A.P. Carapeto, A.M. Ferraria, A.M.B. Do Rego, Unraveling the reaction mechanism of silver ions reduction by chitosan from so far neglected spectroscopic features, Carbohydr. Polym. 174 (2017) 601–609, https://doi.org/10.1016/j.carbpol.2017.06.100.

[32] Z. Adamczyk, G. Para, P. Warszyński, Influence of ionic strength on surface tension of cetyltrimethylammonium bromide, Langmuir 15 (1999) 8383–8387, https://doi.org/10.1021/la990241o.

[33] M.J. Qazi, S.J. Schlegel, E.H.G. Backus, M. Bonn, D. Bonn, N. Shahidzadeh, Dynamic surface tension of surfactants in the presence of high salt concentrations, Langmuir 36 (2020) 7956–7964, https://doi.org/10.1021/acs.langmuir.0c01211.

[34] P. Márton, L. Áder, D.M. Kemény, A. Rácz, D. Kovács, N. Nagy, G.S. Szabó, Z. Hórvölgyi, Chitosan–surfactant composite nanocoatings on glass and zinc surfaces prepared from aqueous solutions, Molecules 29 (2024) 3111, https://doi.org/10.3390/molecules29133111.

[35] A.-L. Kjøniksen, B. Nyström, C. Iversen, T. Nakken, O. Palmgren, T. Tande, Viscosity of dilute aqueous solutions of hydrophobically modified chitosan and its unmodified analogue at different conditions of salt and surfactant concentrations, Langmuir 13 (1997) 4948–4952, https://doi.org/10.1021/la9702594.

[36] H.Y.C. Eulálio, M. Vieira, T.B. Fideles, H. Tomás, S.M.L. Silva, C.A. Peniche, M.V. L. Fook, Physicochemical properties and cell viability of shrimp chitosan films as affected by film casting solvents. I-potential use as wound dressing, Materials 13 (2020) 5005, https://doi.org/10.3390/ma13215005.

[37] A. Garlea, A. Manole, M.I. Popa, V. Melnig, Chitosan-paracetamol nanostructure self-assembling matrices as drug delivery systems, Mater. Plast. 46 (2009).

[38] A. Gârlea, V. Melnig, M.I. Popa, Nanostructured chitosan–surfactant matrices as polyphenols nanocapsules template with zero order release kinetics, J. Mater. Sci. Mater. Med. 21 (2010) 1211–1223, https://doi.org/10.1007/s10856-009-3968-x.

[39] K. He, N. Chen, C. Wang, L. Wei, J. Chen, Method for determining crystal grain size by X-ray diffraction, Cryst. Res. Technol. 53 (2018) 1700157, https://doi.org/10.1002/crat.201700157.

[40] B. Tegze, G. Tolnai, E. Albert, D. Hessz, M. Kubinyi, J. Madarász, Z. May, D. Olasz, G. Sáfrán, Z. Hórvölgyi, Optimizing the composition of LaF_3:Yb,Tm upconverting nanoparticles synthesised by the co-precipitation method to improve the emission intensity, Nanoscale 16 (2024) 21554–21560, https://doi.org/10.1039/D4NR03096F.

[41] W.M. Facchinatto, D.M. dos Santos, A. Fiamingo, R. Bernardes-Filho, S. P. Campana-Filho, E.R. de Azevedo, L.A. Colnago, Evaluation of chitosan crystallinity: a high-resolution solid-state NMR spectroscopy approach, Carbohydr. Polym. 250 (2020) 116891, https://doi.org/10.1016/j.carbpol.2020.116891.

[42] B.K. Lavine, S. Hendayana, Y. He, W.T. Cooper, Solid-state NMR studies of ionic surfactants adsorbed on cyanopropyl bonded phases: implications for micellar liquid chromatography, J. Colloid Interface Sci. 179 (1996) 341–349, https://doi.org/10.1006/jcis.1996.0225.

[43] D. Xu, J. Feng, S. Che, An insight into the role of the surfactant CTAB in the formation of microporous molecular sieves, Dalton Trans. 43 (2014) 3612–3617, https://doi.org/10.1039/C3DT53308E.

[44] Y. Gu, D. Li, The ζ-potential of glass surface in contact with aqueous solutions, J. Colloid Interface Sci. 226 (2000) 328–339, https://doi.org/10.1006/jcis.2000.6827.

[45] J.T. Cabral, J.S. Higgins, T.C.B. McLeish, S. Strausser, S.N. Magonov, Bulk spinodal decomposition studied by atomic force microscopy and light scattering, Macromolecules 34 (2001) 3748–3756, https://doi.org/10.1021/ma0017743.

[46] T. Josyula, L. Kumar Malla, T.M. Thomas, S.S. Kalichetty, P. Sinha Mahapatra, A. Pattamatta, Fundamentals and applications of surface wetting, Langmuir 40 (2024) 8293–8326, https://doi.org/10.1021/acs.langmuir.3c03339.

[47] I. Langmuir, The constitution and fundamental properties of solids and liquids. II liquids, in: H.M. Leicester (Ed.), Source Book Chem. 1900–1950, Harvard University Press, 2013, pp. 123–131, https://doi.org/10.4159/harvard.9780674366701.c50/html (accessed February 4, 2026).

[48] M.K. Chaudhury, Interfacial interaction between low-energy surfaces, Mater. Sci. Eng. R. Rep. 16 (1996) 97–159, https://doi.org/10.1016/0927-796X(95)00185-9.

[49] P. Márton, A. Rácz, B. Szolnoki, J. Madarász, N. Nagy, B. Fodor, P. Basa, J. Rohonczy, Z. Hórvölgyi, Chitosan nanocoatings N-acylated with decanoic anhydride: hydrophobic, hygroscopic and structural properties, Carbohydr. Polym. 343 (2024) 122480, https://doi.org/10.1016/j.carbpol.2024.122480.

[50] B. Jańczuk, W. Wójcik, A. Zdziennicka, Wettability and surface free energy of glass in the presence of cetyltrimethylammonium bromide, Mater. Chem. Phys. 58 (1999) 166–171, https://doi.org/10.1016/S0254-0584(98)00274-0.

[51] S.L. Estes, B. Qiao, G.B. Jin, Ion association with tetra-n-alkylammonium cations stabilizes higher-oxidation-state neptunium dioxocations, Nat. Commun. 10 (2019) 59, https://doi.org/10.1038/s41467-018-07982-5.

[52] X. Zhang, R. Bai, Mechanisms and kinetics of humic acid adsorption onto chitosan-coated granules, J. Colloid Interface Sci. 264 (2003) 30–38, https://doi.org/10.1016/S0021-9797(03)00393-X.

[53] V.K. Paruchuri, A.V. Nguyen, J.D. Miller, Zeta-potentials of self-assembled surface micelles of ionic surfactants adsorbed at hydrophobic graphite surfaces, Colloids

Surf. A Physicochem. Eng. Asp. 250 (2004) 519–526, https://doi.org/10.1016/j.colsurfa.2004.04.098.
[54] C. Akmil Başar, A. Karagunduz, B. Keskinler, A. Cakici, Effect of presence of ions on surface characteristics of surfactant modified powdered activated carbon (PAC), Appl. Surf. Sci. 218 (2003) 170–175, https://doi.org/10.1016/S0169-4332(03)00576-2.
[55] T.J. Silhavy, D. Kahne, S. Walker, The bacterial cell envelope, Cold Spring Harb. Perspect. Biol. 2 (2010) a000414, https://doi.org/10.1101/cshperspect.a000414.
[56] S. Brown, J.P. Santa Maria, S. Walker, Wall teichoic acids of gram-positive bacteria, Ann. Rev. Microbiol. 67 (2013) 313–336, https://doi.org/10.1146/annurev-micro-092412-155620.
[57] S. Buffet-Bataillon, P. Tattevin, M. Bonnaure-Mallet, A. Jolivet-Gougeon, Emergence of resistance to antibacterial agents: the role of quaternary ammonium compounds—a critical review, Int. J. Antimicrob. Agents 39 (2012) 381–389, https://doi.org/10.1016/j.ijantimicag.2012.01.011.
[58] K. Nakata, T. Tsuchido, Y. Matsumura, Antimicrobial cationic surfactant, cetyltrimethylammonium bromide, induces superoxide stress in *Escherichia coli* cells: superoxide stress by surfactant, J. Appl. Microbiol. 110 (2011) 568–579, https://doi.org/10.1111/j.1365-2672.2010.04912.x.
[59] P. Gilbert, A. Al-taae, Antimicrobial activity of some alkyltrimethylammonium bromides, Lett. Appl. Microbiol. 1 (1985) 101–104, https://doi.org/10.1111/j.1472-765X.1985.tb01498.x.